RESEARCH

Laser-induced emission from iron oxide nanoparticles in spray-flame synthesis: in situ high-speed microscopy

Niklas Jüngst[1,3] · Benjamin A. Suedholt[1,3] · Gregory J. Smallwood[2] · Christof Schulz[1,3] ·
Sebastian A. Kaiser[1,3]

Abstract
Spray-flame synthesis uses low-cost precursors dissolved in organic solvents to produce functional metaloxide nanoparticles. In the spray flame, the precursor-laden droplets show frequent and intense thermally-induced disruption, so-called puffing and micro-explosion. This process is often correlated with high uniformity of particle sizes. Whether puffing and micro-explosion are also directly associated with the formation or release of iron oxide nanoparticles is not clear. Also, the spatiotemporal evolution of nanoparticles in the turbulent flow field of the flame is largely unknown from experiments. We performed simultaneous high-speed microscopic imaging of droplet shadowgraphs at 360 kHz as well as elastic light scattering (ELS) and laser-induced emission (LIE) of nanoparticles at 40 kHz. Comparing ELS and LIE images allows distinguishing signals from droplets, flame, and nanoparticles, as only the nanoparticles will appear in images from both methods. ELS and LIE show nanoparticles as thin narrow filaments, presumably following the local flow. Nanoparticle filaments are found at a height of 50 mm and more above the burner in the spray flame. The filaments show increasing LIE signal and higher confinement with increasing height above the burner. The appearance of LIE and thus nanoparticles does not directly correlate with the presence of droplets or their disruption.

1 Introduction

Tailored functional metal-oxide nanoparticles can be produced with spray-flame synthesis (SFS). SFS expands gas-phase synthesis by the application of solutions of solid precursors, e.g., metal salts in combustible solvents. SFS offers the benefit of not requiring vaporizable precursors such as carbonyls and metal-organics that are often toxic, and it extends the range of accessible elements [1]. However, the particle formation route in SFS is much less understood than in gas-phase synthesis from homogeneously mixed gases because of the intricate interplay of droplet evaporation and combustion, with related chemical decomposition and accumulation processes inside the evaporating droplets [2]. There

is a competition between particle formation inside the droplet (droplet-to-particle process) and particle formation from the gas-phase from fully evaporated species (gas-to-particle process) [3]. These competing processes may lead to the formation of material mixtures with a combination of microscale and nanoscale particles from the respective processes [4]. It is unknown, however, which species evaporate from the droplet into the gas phase to then enable gas-to-particle formation. Therefore, also subsequent gas-phase reactions as well as the particle-forming species are not known. Previous works have shown puffing and micro-explosion, i.e., disruption, of precursor-laden droplets [5–7], which both help in quickly bringing the precursor into the gas phase and thus resulting in the desired nano-powders with narrow size distributions. So far it is not clear whether nanoparticles form in the direct vicinity of disrupting droplets, the disruption process releases particles previously dispersed in the liquid as a result of precipitation, or the appearance of droplets and nanoparticles is spatially uncorrelated. Clarification of this question requires simultaneous in situ visualization of droplets and nanoparticles. Such combined measurements can additionally aid in understanding the nanoparticle formation

✉ Niklas Jüngst
niklas.juengst@uni-due.de

1   Institute for Energy and Materials Processes, University of Duisburg-Essen, Duisburg, Germany

2   Metrology Research Centre, National Research Council Canada, Ottawa, ON, Canada

3   Center for Nanointegration Duisburg-Essen, CENIDE, University of Duisburg-Essen, Duisburg, Germany

routes and turbulence–droplet–particle dynamics. However, such data is to date virtually nonexistent from experiments.

Most documented optical in situ measurements focus on point measurements of nanoparticle volume fraction or size during synthesis via light scattering techniques [8–10], laser-induced incandescence (LII) [11–15], and phase-selective laser-induced breakdown spectroscopy (ps-LIBS) [16–18]. Small-angle X-ray scattering [8] and wide-angle light scattering [9, 10] were used to measure the size evolution of titania and iron oxide nanoparticles in SFS as a function of the height above the burner (HAB). LII was originally conceived for soot but can also be used for the detection of non-soot particles, e.g., metals and metal oxides [11]. Here, challenges lie in low absorption cross-sections and boiling temperatures of these materials and - particularly for metal oxides - the unknown phase and composition changes during laser heating [11, 15, 19]. In the gas-phase synthesis of iron oxide nanoparticles from iron pentacarbonyl as precursor, LII was used to determine particle volume-fractions [13] and sizes [14]. Time-resolved measurements found the LII decay time to be only 100–200 ns long [13]. Atomic emission of iron was detected via ps-LIBS as a function of HAB in SFS of iron oxide nanoparticles from iron(III) nitrate nonahydrate ($Fe(NO_3)_3 \cdot 9H_2O$, INN) dissolved in various solvents [16]. The signal from aerosolized titania nanoparticles excited at 355 nm was acquired with spectral and temporal resolution [12]. For laser fluences below 0.1 J/cm^2, the signal was dominated by photoluminescence, as validated by a narrow emission spectrum at around 470 nm. Delaying the detection gate prevented the detection of photoluminescence. A transition towards dominating incandescence signals was found with increasing laser fluence [12]. However, also atomic emissions and bremsstrahlung (both from ps-LIBS) interfered with the LII signal even at low to moderate fluences [12, 20]. In a flame, evaporation of species from the hot particles and their subsequent excitation, e.g., via the reaction with surrounding radicals, might lead to additional signal interference from chemiluminescence [21]. Therefore, the term laser-induced emission (LIE) [12] has evolved for a signal that is indicative for the presence of particles without referring to a specific process of signal generation.

Only very few studies report in situ two-dimensional visualization of nanoparticle spatial distributions in gas-phase synthesis. Ensemble averages of single-shot ps-LIBS [22, 23] and LII [15] show the titania distribution in gasphase synthesis from vapor-fed titanium isopropoxide in laminar diffusion flames. Recently, resonanceenhanced instantaneous ps-LIBS imaging was used to determine the spatial distribution of titania which was found to be most concentrated in highly wrinkled structures in the turbulent flame [24]. This is consistent with recent large-eddy simulations of iron oxide nanoparticle formation in SFS [25, 26] and direct numerical simulations of titania formation in gasphase synthesis [27]. Aerosolized droplets of INN dissolved in 1-butanol were fed into the flame of a low-pressure laminar matrix burner to investigate the interaction of INN-based products on the flame chemistry in the absence of droplets and turbulence [28]. Here, elastic light scattering (ELS) signals from nanoparticles were found in vertical streaks originating from the outflow orifices of the burner. The authors proposed that particle formation started from INN residue as a leftover from evaporated droplets, followed by pyrolysis and surface reactions to iron oxide nanoparticles in the gas phase [29–31]. Experimental work on in situ visualization of nanoparticle formation in the surrounding of droplets in SFS is not known to us.

The aim of this work is to visualize nanoparticles during SFS from combustible INN solution droplets. Specifically, we want to visualize their spatiotemporal appearance in the turbulent reacting flow field. We also aim at finding out whether we can see nanoparticles being ejected into the surrounding gas phase during droplet puffing or micro-explosion. This would be a direct proof of particle precipitation in the liquid phase or rapid nucleation from the gas phase.

2 Methods

2.1 Spray-flame synthesis

Figure 1 shows a schematic overview of the "SpraySyn" [32] burner that is used for SFS of iron oxide nanoparticles.
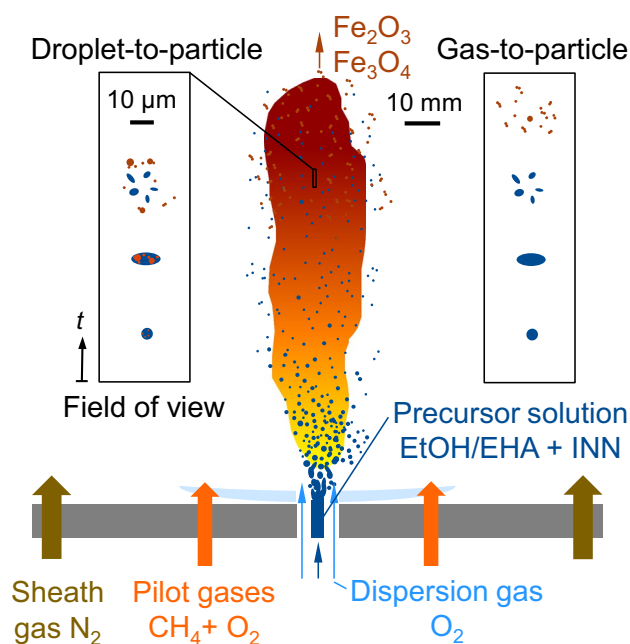

Fig. 1 SpraySyn burner and nanoparticle formation routes

Precursor-laden solvents are fed through a central capillary (2 ml/min, 0.26 m/s nominal exit velocity) and atomized in a two-fluid nozzle by a fast co-annular oxygen flow (10 slm, 120 m/s, nozzle-exit velocity, nozzle-exit Reynolds number 7160 [33]). INN was dissolved in a mixture of 35% ethanol (EtOH) and 65% 2-ethylhexanoic acid (EHA, $C_8H_{16}O_2$). Catalyzed by dissolved Fe ions, the two solvent components partially react to 2-ethylhexanoate (EH) [4]. The Fe ions then react with EH to the complex iron(III) 2-ethylhexanoate (Fe-EH). The combustion of the fine spray was stabilized by a pilot flame of premixed methane (2 slm) and oxygen (16 slm) that had an exit velocity of 2.3 m/s. From a 70-cm diameter sintered metal plate, nitrogen surrounded the flame as a sheath gas with a flow rate of 120 slm (exit velocity 0.6 m/s). Below 20 mm HAB, the spray undergoes primary and secondary atomization while further downstream the droplets are subject to frequent puffing and micro-explosion events [34].

Figure 1 schematically shows the droplet-to-particle and gas-to-particle processes in the context of droplet disruption in SFS. As the temperature of the INN-laden droplets increases, Fe-EH tends to decompose, which might result in the precipitation of iron hydroxide nanoparticles within the droplets. Those can accumulate near the droplet surface and initiate superheating and bubble nucleation, resulting in puffing or micro-explosion [34, 35]. On the other hand, evaporated iron is expected to form molecular water-rich iron oxides that then nucleate towards nanoparticles [36]. Products from SFS in this configuration are γ-Fe_2O_3, Fe_3O_4, and to a lesser extent α-Fe_2O_3 (determined ex situ from sampled powder via X-ray diffraction [16] and the lattice geometries in high-resolution transmission electron microscopy [37]). Therefore, the particle species being probed in situ is not known and might be a condensed-phase intermediate. It might even be different from the ones mentioned above.

2.2 Optical diagnostics

With the diagnostic approach in this work, our objective is to image nanoparticles and droplets in spray-flame synthesis. The simultaneous measurement of LIE and ELS enables the distinction of droplets (only visible in ELS images) and flame luminosity (only visible in LIE images) from nanoparticles that are visualized via both ELS and LIE. This enables an unambiguous identification of nanoparticles in LIE and ELS images, as further discussed in Sect. 2.3. Shadowgraphy shows droplets, their disruption, and the resulting droplet fragments.

Figure 2 shows the optical layout for visualizing nanoparticles and droplets in SFS. For the excitation of LIE and ELS, a high-repetition-rate Nd:YVO$_4$ laser (Edgewave IS335, 532 nm, 1.7 mJ/pulse) was operated at a pulse repetition rate of 40 kHz. A cylindrical lens ($f = 50$ mm)
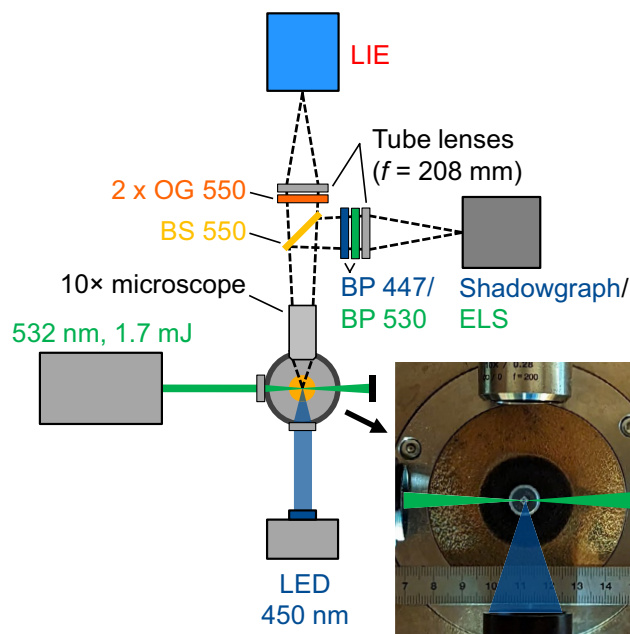

Fig. 2 Optical layout of high-speed shadowgraphy, laser-induced emission (LIE), and elastic light scattering (ELS)

focused the beam horizontally. To determine the thickness of the beam waist, a vertical slit aperture was horizontally translated in 10 μm steps through the focused beam. The remaining laser pulse energy behind the aperture was measured with a power meter. This showed a thickness of 70 μm (laser pulse energy dropped to less than 1% of the maximum value). An aperture clipped the beam vertically such that a height of 5 mm in the spray was illuminated. This yielded a laser fluence of 5 mJ/mm^2 in the field-of-view. The absorption function of Fe_2O_3 is 0.08 at 532 nm, as derived from [11, 38], and thus about five times lower than that for soot at this wavelength [19].

During the excitation of LIE, the liquid nanoparticles are heated to their boiling temperature (e.g., $T_{b,Fe} = 3134$ K [39]). In addition to the fact that the particle species being probed is unknown, other uncertainties evolve from laser interaction with the particulate material. The higher the temperature, the more iron oxide nanoparticles are expected to phase-shift to less oxidized states, e.g., from Fe_3O_4 to FeO [11, 40]. Laser heating of the particles might additionally result in phase changes with fixed composition, i.e., γ-Fe_2O_3 $\rightarrow$ α-Fe_2O_3 [11, 41]. Whether such phase changes are fast enough to occur during the nanosecond timescale of laser heating is not clear.
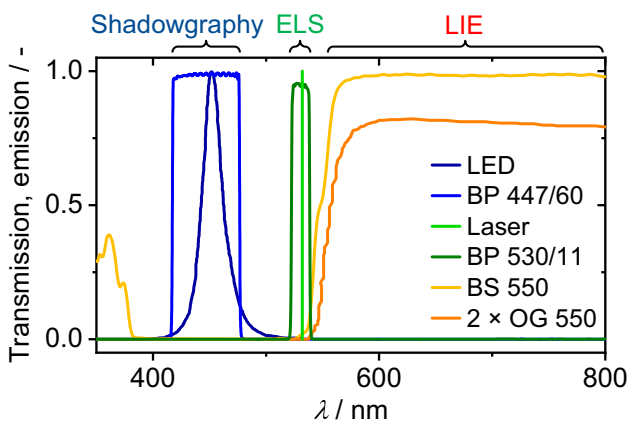
For the visualization of droplet shadowgraphs, a blue light-emitting diode (Cree XP-E2 SMD LED, 550 mW, 450 nm) was pulsed by a commercial driver (Picolas LDP-V 50–100 V3.3). The pulse duration was on the order of 100 ns [34]. The LED pulse was formatted with a Köhler-like

arrangement for local and homogeneous illumination of the field-of-view [6].

A microscope (Mitutoyo M Plan Apo 10×) collected LIE, ELS, and transmitted LED light. The photo in Fig. 2 shows the ends of the lens tubes for both illuminations, the microscope objective, and a syringe needle ($d = 250$ μm) as a target from above the SpraySyn burner. Behind the microscope lens, the images are in infinity space with nearly parallel rays.

A beam splitter (Thorlabs, DMLP550L) transmitted light with a wavelength above 550 nm (LIE) and reflected light with a shorter wavelength (ELS or LED light). To separate the LIE signal in the transmitted light from leaking ELS and LED light, two 3-mm thick orange-glass longpass filters (Schott, OG550) were placed behind the beam splitter. This way, the transmission at 450 nm (center wavelength of the LED) and 532 nm became 3×10^{-11} and 4×10^{-7}, respectively. The transmitted LIE signal was then imaged by a tube lens onto an intensified (LaVision, HS-IRO) high-speed camera (Vision Research, Phantom VEO 710). The reflected portion of the light - either LED light for shadowgraphy or ELS - was spectrally isolated with corresponding bandpass filters (Semrock, 447/60 BrightLine and 530/11 BrightLine). A second tube lens imaged the reflected filtered signal onto the sensor of a second non-intensified high-speed camera (Photron, SA-Z). Figure 3 summarizes the spectral characteristics of light sources and detection for LIE, ELS, and droplet shadowgraphy.

Figure 4 shows the temporal features of the measurements. For the simultaneous imaging of LIE and ELS, the frame rates of both the intensified high-speed camera and the non-intensified one were synchronized with the laser at $f_{laser} = 40$ kHz. The gate of the intensified high-speed camera was $t_{gate} = 300$ ns and the exposure time of the non-intensified camera was $t_{HSC} = 25$ μs.
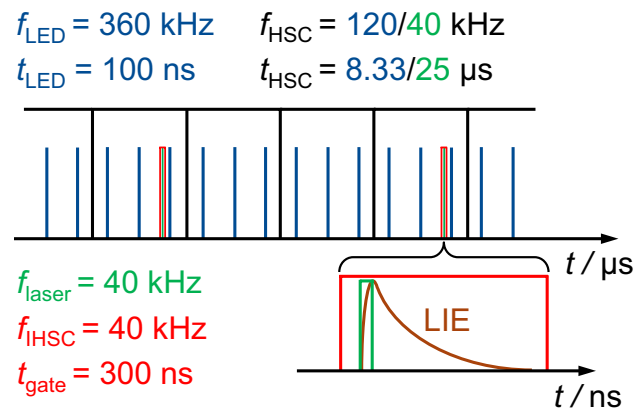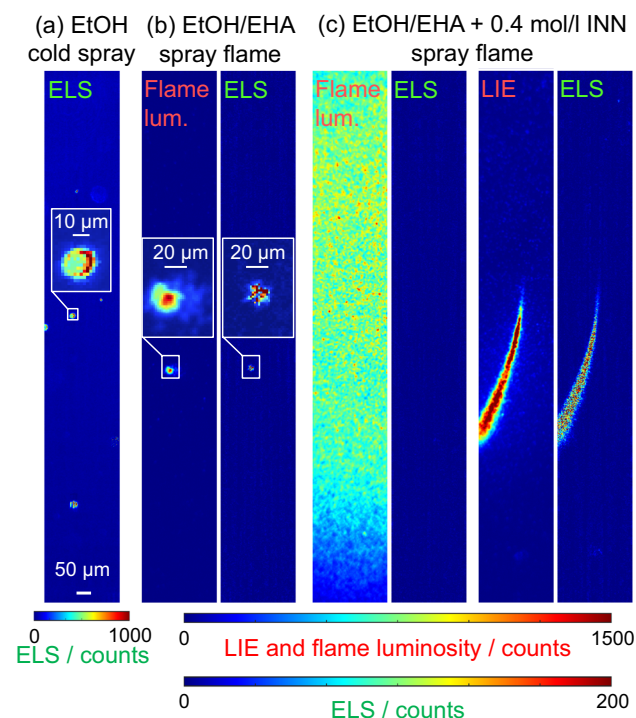

Fig. 4 Measurement sequence of shadowgraphy (blue), elastic light scattering (ELS, green), and laser-induced emission (LIE, brown). The repetition rate and exposure time of the non-intensified high-speed camera (HSC) are marked in black, the intensifier gate time and the repetition rate of the intensified high-speed camera (IHSC) in red

For simultaneous imaging of LIE and shadowgraphs, the frame rate of the non-intensified camera for shadowgraphy was increased to $f_{HSC} = 120$ kHz while the exposure time was reduced to $t_{HSC} = 8.33$ μs. The LED was triggered at $f_{LED} = 360$ kHz such that three nearly equally spaced droplet shadows were stacked in each frame. The repetition rate of the intensified camera at 40 kHz was three times and nine times lower than those of the non-intensified camera and the LED, respectively. Thus, one LIE image was acquired per nine droplet shadows. The laser was triggered 100 ns before the ninth droplet shadow.

2.3 Interference mitigation and imaging strategy

To identify and distinguish droplet-related ELS and flame luminosity from nanoparticle-related signals, preliminary measurements were performed. Figure 5a shows an ELS image acquired in a cold ethanol spray. The laser beam is incident from the left. As no signal was found in the corresponding LIE image (for all 135,000 image pairs), none is shown. The ELS image shows scattered light from ethanol droplets. Total internal reflection on the right interior of the droplet causes the signal there to be highest.

In a spray flame of EtOH/EHA without INN, signal in the LIE image, Fig. 5b left, was detected. As elastically scattered light was not found in the LIE images in the cold spray, this signal is attributed to flame luminosity, i.e., chemiluminescence, and not LIE, which is not expected in the absence of particles. The ELS inset shows a spatially strongly inhomogeneous signal across the droplet. The interaction of the droplet with the light sheet further upstream can cause laser-induced fragmentation of the droplet (see Sect. 3.2), resulting in such signal distribution. This process causes the quick release of fuel vapor leading to strong flame luminosity. For

Fig. 3 Transmission curves of filters and beam splitter as well as spectral characteristics of light sources

Fig. 5 Elastic light scattering (ELS), laser-induced emission (LIE), and flame-luminosity images from **a** a cold EtOH spray at 60 mm HAB and spray flames of **b** EtOH/EHA and **c** EtOH/EHA + INN at 70 mm HAB. The two image pairs from the INN-laden flame were acquired at different times

flames without INN, the majority of the image pairs show droplet-related ELS, and in the corresponding LIE images, there is no interference from flame luminosity.

Visually, in a spray flame operated with EtOH/EHA with 0.4 mol/l INN, Fig. 5c, the flame luminosity significantly increases compared to the cases without INN. This additional signal interference is attributed to chemically- and thermally-excited iron-containing intermediates in the gas phase as well as Planck radiation from nanoparticles. The first image pair of ELS and LIE from the precursor-laden spray flame shows an example of this flame luminosity, sometimes interfering in the LIE image and covering the entire field-of-view. As the spray flame fluctuates in time and space, flame luminosity is not observed in every image. Flame luminosity is not detected in the ELS image. In addition to global and local flame luminosity in INN-laden spray flames, sharply elongated filaments are found in the LIE and ELS images as shown in Fig. 5c right. The position and shape of the detected filaments agrees well in both images. Such filaments are never found in a spray flame without INN, which indicates that those filaments are not related to potentially formed soot, as the flame becomes even leaner by the addition of INN. Also, flame pulsation, resulting in locally fuel-rich zones and

thus potential soot formation, is known to be of similar frequency for precursor-laden and solvent-only flames [42]. Finally, the filaments are not found in a spray flame of EtOH/EHA + INN without laser excitation. Therefore, the filaments are considered to be related to nanoparticle LIE and ELS. If the detection gate is delayed by only 50 ns relative to the laser pulse, the LIE signal is lost. This suggests that the signals are due to LII from very small particles or due to luminescence of laser-evaporated molecular or atomic species. Flame luminosity from an INN-laden spray flame (0.5 mol/l INN in EtOH) was detected with spectral resolution as a function of HAB by Prenting [43]. The spectra indicate strong broad-band thermal radiation from iron-oxide nanoparticles with several distinct lines superimposed. After subtraction of the thermal radiation (fitting the continuous part of the spectrum), strong emission from FeO^* (between 550 and 650 nm) was identified. As this emission between 550 and 650 nm lies within our LIE detection filter-band, the luminescence of laser-evaporated species can be attributed to coming from FeO^* and other intermediates emitting in this spectral region.

40,000 LIE and ELS image pairs were acquired at 70 mm HAB, i.e., far downstream in the spray flame. At this height, the interference by flame luminosity is much weaker than at lower HAB. Also, the droplet number concentration in this zone is low and gas velocities are lower (about 60 m/s). The latter enables following the nanoparticle filaments over multiple frames. Then, droplet shadowgraphs and LIE were simultaneously imaged. In the simultaneous imaging of droplet shadowgraphs and LIE, 150,000 shadowgraphy and 50,000 LIE images were acquired in each measurement. Measurements were carried out with solutions containing 0.4 mol/l INN at 40, 50, 60, and 70 mm HAB and 0.2 mol/l INN at 50 and 70 mm HAB. All measurements were done on the centerline of the spray flame.

To select the LIE images showing nanoparticles from all acquired images, automatic processing and visual inspection were performed. From all acquired LIE images in a measurement series, the ones having 200 pixels or greater with more than 200 counts were, together with the corresponding ELS or shadowgraph images, automatically selected for further analysis. 200 pixels correspond to a circular area-equivalent diameter of 28 µm, a relatively large droplet. In this size range and below, a flame surrounding a droplet cannot be distinguished from LIE. The threshold of 200 counts is about 12 times above the dark noise of the intensified high-speed camera (standard deviation of 16 counts) and yields a (visually) acceptable signaltonoiseratio of the nanoparticle filaments. From those sets of pre-processed images, the ones containing nanoparticle filaments were identified and extracted by visual inspection.

3 Results

3.1 Nanoparticle LIE and ELS

Figure 6 shows image pairs of (left) LIE and (right) ELS from nanoparticles at 70 mm HAB. Nanoparticle filaments are located in very similar regions in each image pair. Despite the relatively weak signal-to-noise ratio, both methods clearly show these long, thin structures. Their apparent transverse width ranges from 5 to 50 μm. It is not clear whether filaments that appear wider really have
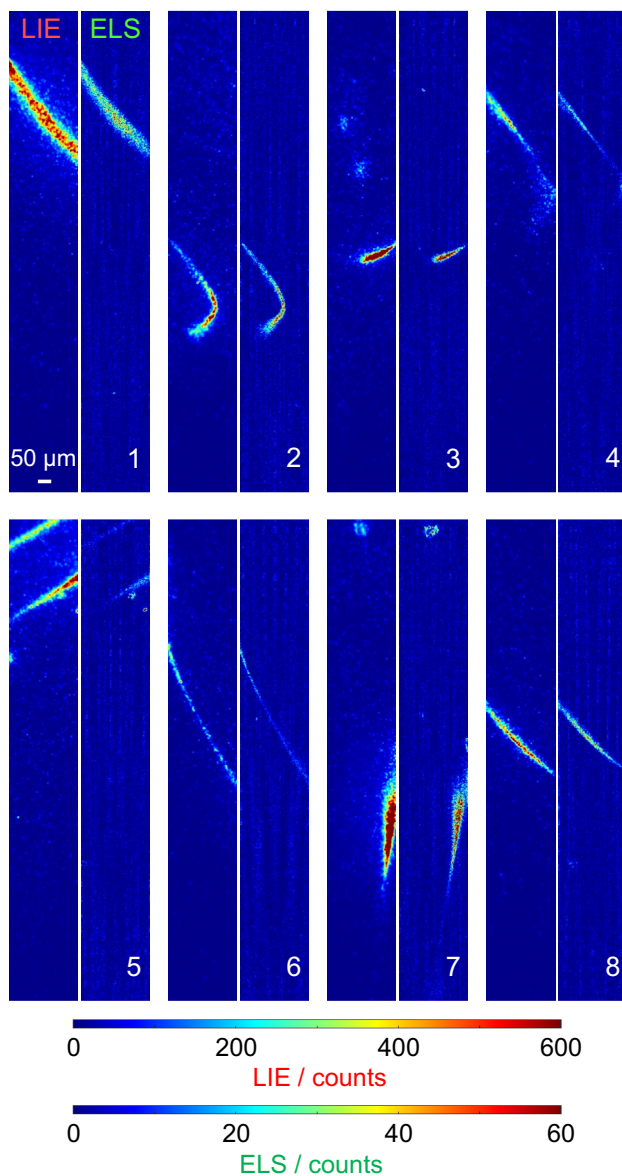
a greater physically width or appear widened because the two-dimensional light sheet is intersecting a nanoparticle sheet that is not orthogonal to the light-sheet plane, an effect that is well known from imaging of scalar dissipation layers [44, 45] and soot sheets [46]. Note that the visible depth of the filaments perpendicular to the image plane is limited by the light sheet thickness of 70 μm. Image pairs 1, 4, 5, 6, and 8 show the filaments even extending over the whole 250 μm width of the field-of-view, most likely in eddies of several hundred micrometers in size. In contrast to this, the curved filament in the second frame in Fig. 6 is consistent with an eddy of 50–100 μm in size.

The observation of thin wrinkled nanoparticle-laden filaments is very similar to LII visualizations of soot in turbulent jet flames [47–50]. The high Schmidt number Sc of the particles causes them to follow local eddies in the turbulent flow rather than diffusing out into the surrounding field, i.e., the Kolmogorov scale l_K (the smallest eddy size) is much larger than the Batchelor scale l_B (the smallest size of scalar structures), since $l_K/l_B = Sc^{1/2}$ [51]. In studies of soot formation, laser-induced fluorescence of gas-phase soot precursors showed regions with much less of this narrow shape, and in fact, these PAH have a much higher diffusivity than nanoparticles [47, 49]. A direct numerical simulation of titania formation from the gas phase showed a decrease in the filament thickness with increasing particle size as the nanoparticles' diffusivity decreases and the viscosity increases (Sc is about 4000 for nanoparticles with diameters around 30 nm) [27]. Finding nanoparticles in elongated filaments is also consistent with recent large-eddy simulation of nanoparticle formation in SFS [25, 26]. However, in these simulations the mesh resolution of 125 μm per cell could not resolve structures of the size that we see in our images.

Figure 7 shows four sequences of nanoparticle LIE from consecutive images. In each sequence, consecutive images were spatially superimposed with a dashed white line indicating the transition between two images. That way the spatiotemporal evolution within the field-of-view is clearer.

Sequence 1 shows a counterclockwise rotation of the LIE filament. This apparent nanoparticle transport may correspond to in-image-plane convection or to out-of-plane convection of the underlying three-dimensional nanoparticle sheet. The filament in sequence 2 stretches and becomes thinner throughout the field-of-view, indicating locally compressive flow. Sequences 3 and 4 show straight filaments, angled at about 45°, showing the transport of LIE towards the "top" of the filament. The fact that we find filaments in multiple consecutive images shows that the laser energy input does not entirely vaporize them or induce a breakdown with a single laser irradiation.
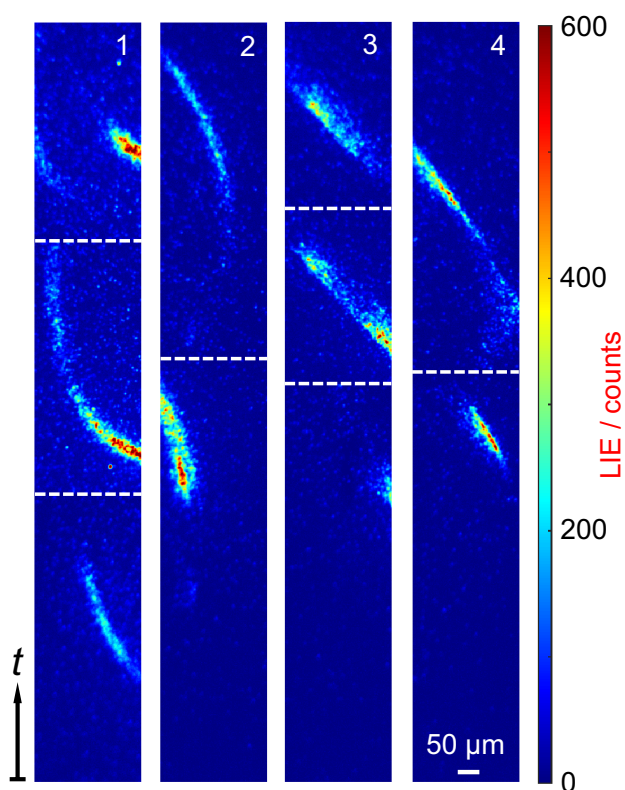

Fig. 6 Selected image pairs of (left) laser-induced emission (LIE) and (right) elastic light scattering (ELS) from iron oxide nanoparticles at 70 mm HAB using solutions containing 0.4 mol/l INN

Fig. 7 Consecutive images of laser-induced emission (LIE) acquired at 70 mm HAB using solutions containing 0.4 mol/l INN.

3.2 Droplet shadowgraphs and LIE

Figure 8 shows three consecutive sequences of droplet shadowgraphs and LIE images. The sequences were acquired with solutions containing 0.4 (sequence 2) and 0.2 mol/l INN (sequences 1, 3). The corresponding HAB are indicated in the caption. With the LIE imaging, the interaction of the light sheet with the droplets and the resulting droplet disruption affected the measurements. The INN-laden droplets (to the eye they are orange in color) strongly absorb green laser light. Since the droplets also act as micro lenses, local fluences far above 0.5 J/cm^2 are expected to be reached, leading to local superheating, resulting in bubble nucleation, growth, and micro-explosion. This process is visible in the first shadowgraphy image in both sequences 1 and 3. The laser is triggered 100 ns before the third LED pulse whose resulting droplet shadow already shows droplet expansion and disintegration. According to Ref. [52], the high laser fluence can result in laser-induced breakdown of the dissolved precursor. However, as the atomic iron emission is at wavelengths shorter than 550 nm, this is not expected to optically interfere.

In sequence 1, the cloud of droplet fragments, generated by the interaction with the light sheet, moves downstream and evaporates or becomes defocused. Both laser-illuminated images at 0 and 25 µs do not show nanoparticle LIE but only globally distributed weak flame luminosity. Sequence 2 shows two droplets with the lower one puffing over the entire sequence. Since the droplet is defocused at 0
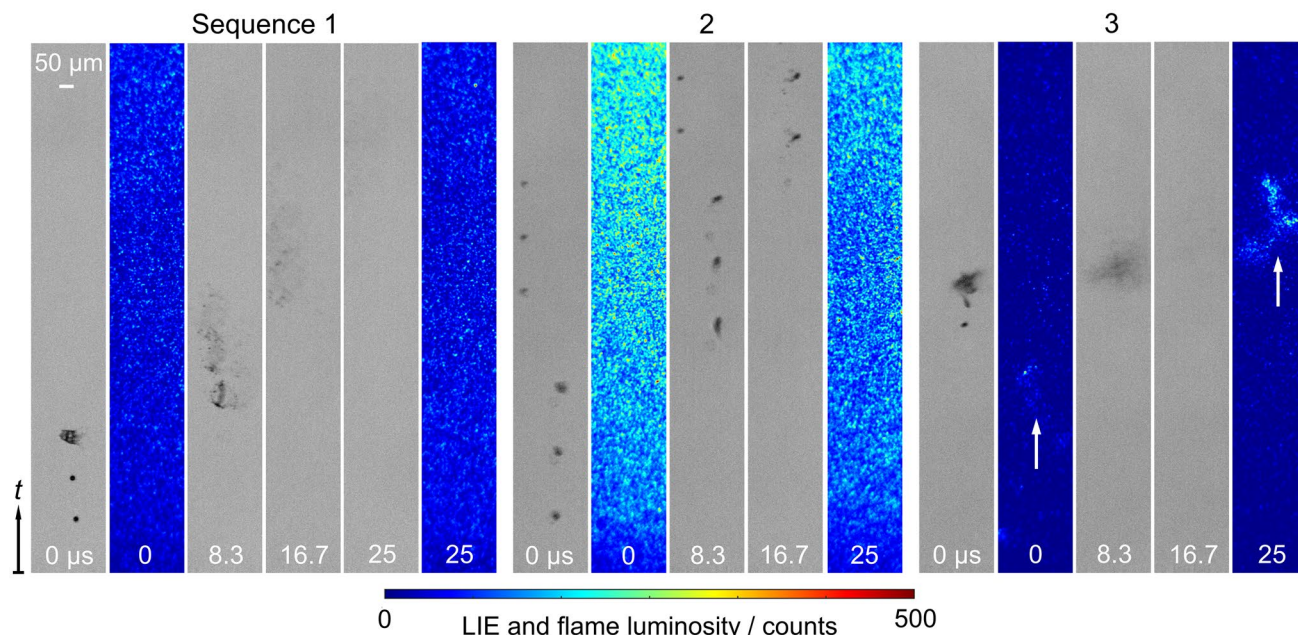
Fig. 8 Consecutive images of droplet shadowgraphs and laser-induced emission (LIE) or flame luminosity at 50 mm HAB (sequences 1, 2) and 70 mm HAB (sequence 3). White arrows indicate potential nanoparticle LIE.

μs, it most likely does not interact with the light sheet at that time and continues in its 'natural' disruption. Also in this sequence, solely global flame luminosity, stronger here than in sequence 1, is detected in the laser-illuminated images at 0 and 25 μs. The shadowgraphy image at 25 μs is not shown as the droplets have left the field-of-view.

In sequence 3, the droplet appears to be puffing, i.e., deforming and ejecting a secondary droplet to the side, presumably before being exposed to the light sheet. The third droplet shadow at 0 μs shows it expanding and fragmenting. The image at 8.3 μs shows a cloud of fine fragments which evaporate quickly. At 25 μs, weak signal is found in the laser-illuminated image at approximately the height where the evaporated fragments are at that time (shadowgraphy image at 25 μs empty and thus not shown). The wrinkled morphology of the signal is very different from local flame luminosity, which is much smaller and rather spherical, as exemplarily shown in Fig. 5b left. It thus most likely can be attributed to nanoparticle LIE. Those nanoparticles might either be condensed from gas-phase species or directly ejected during the micro-explosion of the droplet. As weak signal also arises upstream of the droplet at 0 μs, formation from the gas phase is more likely. We note that sequence 3 shows rather an exception and the observations from sequences 1 and 2 are more representative for what is seen in the simultaneous visualization of droplets and LIE, independent of the HAB or INN concentration.

These results indicate that the presence of droplets and droplet disruptions does not correlate with the detection of nanoparticle LIE in the close vicinity. This could have several reasons. First, particle-forming species that emanate from a droplet might require longer time for particle nucleation than the observation time, limited by the passage of the droplet across the field-of-view (about 20 μs). Particles would then be formed more uniformly throughout the flow. Second, shortcomings of the measurement technique might prevent the detection of particles near droplets. In that respect, in our previous work, we reported the precipitation of particles within the droplet as one reason for disruption [34, 35]. However, the precipitating species is iron hydroxide whose absorption at 532 nm in the flame might be much lower than the one of iron oxide. Finally, the number of particles produced from a single droplet or its disruption might simply be too low to generate LIE signal above the darknoise level.

3.3 Nanoparticle evolution in the spray flame

Figure 9 shows representative images of nanoparticle filaments at 50 and 60 mm HAB. Filaments at 50 mm HAB have weaker LIE signal above the luminous background than those at 60 and 70 mm HAB. Also, filaments at this HAB tend to blur out to the sides more than those at higher
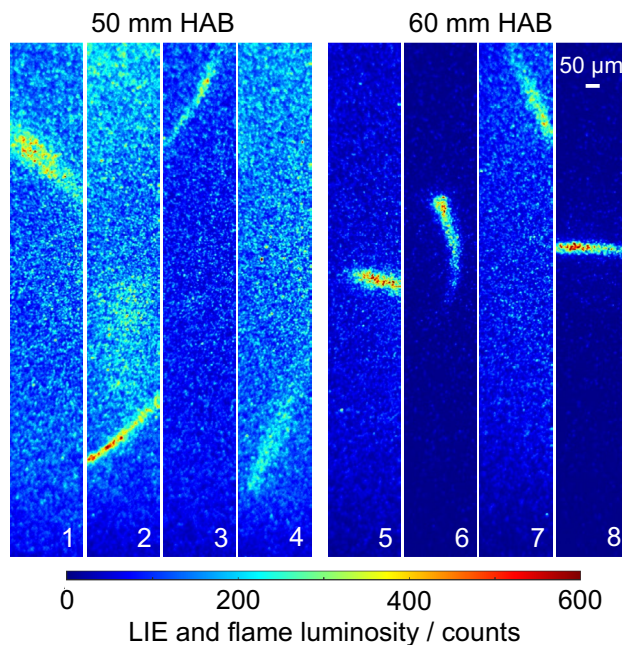
Fig. 9 Laser-induced emission (LIE) images acquired at 50 and 60 mm HAB, from solutions containing 0.4 mol/l INN

HAB. This indicates that nanoparticles here are smaller and are more diffusive. This is consistent with the results presented in Refs. [8, 37], where iron oxide nanoparticles were sampled at different HAB in the same burner configuration and operating condition as in this work. Primary particles with diameters of less than 10 nm were found in transmission electron microscopy images of samples extracted thermophoretically at 50 mm HAB. This suggests that particle nucleation and growth are initiated at around this HAB. Nanoparticle volume fractions are thus low at this HAB, which is reflected by the weak LIE signals.

At 60 mm HAB, filaments become thinner than the ones at 50 mm HAB, indicating decreasing diffusivity of the nanoparticles as growth and agglomeration preferentially occur in the areas with high particle density. The particle volume fraction increases, resulting in increasing LIE signal. At 70 mm HAB, as shown in Fig. 6, the filaments show the highest levels of LIE signal and spatial confinement.

Figure 10 shows the number concentration of nanoparticle filaments, counted by visual inspection, for two different precursor concentrations versus the HAB. The filament number concentration was calculated by counting all filaments in a measurement, e.g., among 50,000 images, and dividing the sum by the total measurement volume, e.g., of 50,000 images (details on the measurement-volume calculation are provided in Ref. [34]). Also shown is the mean droplet number concentration, taken from Ref. [34], versus the HAB. In the experiment with solutions containing 0.4 mol/l INN, nanoparticle LIE is not found below 50 mm
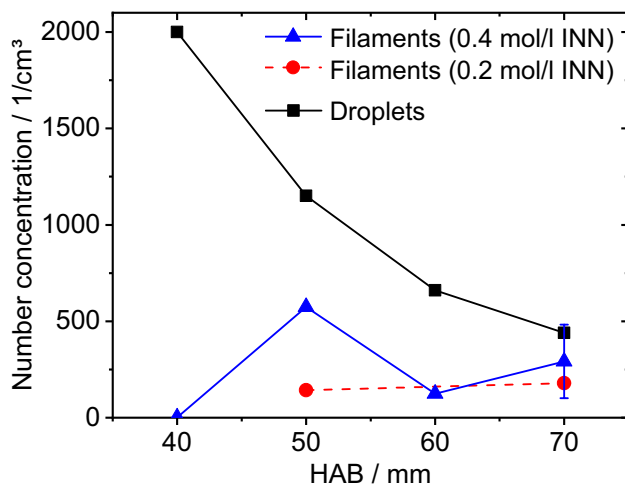
Fig. 10 Filament and droplet number concentrations as a function of HAB for experiments with solutions containing 0.2 and 0.4 mol/l INN. Mean droplet number concentration taken from [34]. The error bar at 70 mm HAB and for a solution containing 0.4 mol/l INN is the standard deviation among two measurements

HAB, qualitatively consistent with the results presented in Refs. [8, 37]. At 50 mm HAB, the number concentration becomes maximal with about 570 filaments/cm^3. With increasing HAB, the turbulence length scales decrease and entrainment of gas from the surrounding widens the spray flame so that filaments become larger and fewer in number. The number concentration decreases to an average of 210 filaments/cm^3 between 60 and 70 mm HAB.

At 0.2 mol/l INN, LIE images were acquired at 50 and 70 mm HAB. Here, the filament number concentration at 50 mm HAB is about three times lower than the one with 0.4 mol/l INN. Also, LIE-signal levels (not shown here) are on average lower for solutions containing 0.2 mol/l INN than in the ones containing 0.4 mol/l INN. As reduced precursor concentration yields smaller final particle sizes [53], the nanoparticle volume fraction in the spray flame is also expected to be reduced, explaining reduced LIE signals in filaments, which are then found less in visual inspection. Also, droplets containing 0.2 mol/ INN were found to have significantly lower probabilities for puffing and micro-explosion than the ones containing 0.4 mol/l INN [34]. This reduces both the evaporation of precursor species and the potential ejection of precipitates into the gas phase. Therefore, solutions with lower INN concentration not only provide less precursor for nanoparticle formation but also reduce the transfer of the precursor and nanoparticles into the gas phase. However, filament number concentrations become surprisingly similar at 70 mm HAB for the two precursor concentrations.

Over the entire examined height of the spray flame, the droplet number concentration is higher than the filament number concentration. The large majority of droplets evaporates below 50 mm HAB, where filaments are not found.

Combining this with the findings from Sect. 3.2 we conclude that nanoparticle filaments are the result of particles produced from multiple droplets that evaporated or disintegrated outside the field-of-view. This is consistent with the spray burning in group combustion, not single-droplet combustion. However, a single droplet may produce one or even more filaments with low nanoparticle volume fraction, which we do not detect due to the limitations of the measurement technique. Also, small nanoparticle structures cannot unambiguously be distinguished from the flame luminosity of droplets.

4 Conclusions

A multi-scalar high-speed microscopy technique was developed to simultaneously visualize droplets and iron oxide nanoparticles in spray-flame synthesis. In this flame, droplets doped with iron(III) nitrate nonahydrate as a precursor had been found to undergo frequent puffing and micro-explosion events, i.e., droplet disruption [7, 34]. A pulsed blue LED illuminated the spray and a microscope imaged the droplets' shadows onto the sensor of a high-speed camera. Laser pulses at 532 nm were formed into a light sheet illuminating the field-of-view from the side. Elastic light scattering (ELS) and laser-induced emission (LIE) from nanoparticles were imaged with the microscope in situ in the flame of the SpraySyn burner onto the sensors of two high-speed cameras.

The combination of ELS (imaging droplets and nanoparticles) and LIE (imaging flame luminosity and nanoparticles) plus the imaging in a precursor-free spray flame enabled the unambiguous identification of nanoparticles in the images. Nanoparticle LIE and ELS were found as thin - 5–50 µm thick - curved filaments, presumably following local eddies in the turbulent flow. Short LIE lifetimes of around 50 ns suggest that the source of signal generation is likely the luminescence of laser-evaporated species or LII of small particles. However, single filaments were sometimes imaged in multiple consecutive LIE images, indicating that filaments are not entirely evaporated during a single laser irradiation.

In a second pairing of the diagnostics, LIE was visualized simultaneously with droplet shadowgraphs. The presence of droplets or their disruptions was not found to be correlated with the appearance of nanoparticle filaments nearby. This suggests that iron oxide nanoparticles predominantly form via the gas-to-particle route. However, low nanoparticle volume fractions and weak absorption functions of intermediate particle-species might hinder the detection of LIE near droplets and disruptions.

Nanoparticle filaments are not found below 50 mm HAB in the spray flame, but it is known that the vast majority of

droplets evaporates and disrupts below 50 mm HAB. This suggests that nanoparticle nucleation and filament formation require several hundred microseconds in the spray flame. With increasing HAB in the spray flame, nanoparticle filaments become less in number, thinner, and show increasing LIE signal. The evidence suggests that for a filament to be visible in the LIE images, multiple evaporating droplets, mixing, and subsequent gas-phase reactions may have contributed particles to a single filament.

Author contributions All authors contributed to the research design. The research was performed by Niklas Jüngst and Benjamin Suedholt. All authors contributed to the discussion and analysis of the results. The first draft of the manuscript was written by Niklas Jüngst and all authors commented on previous versions of the manuscript. All authors read and approved the final manuscript.

Data availability Data will be made available on request.

Declarations

Conflict of interest Non-financial interests: Christof Schulz is on the editorial board of Applied Physics B and receives no compensation as member of the editorial board.

References

1. L. Mädler, H.K. Kammler, R. Mueller, S.E. Pratsinis, J. Aerosol Sci. **33**, 369 (2002)
2. M.R. Lalanne, S.A. Mujaddadi, P. Fjodorow, S. Cheskis, H. Somnitz, I. Wlokas, J. Herzler, M. Fikri, C. Schulz, I. Rahinov, Appl. Energy Combust. Sci. **15**, 100184 (2023)
3. R. Strobel, S.E. Pratsinis, Phys. Chem. Chem. Phys. **13**, 9246 (2011)
4. S. Angel, J. Neises, M. Dreyer, K. Friedel-Ortega, M. Behrens, Y. Wang, H. Arandiyan, C. Schulz, H. Wiggers, AlChE J. **66**, 16748 (2019)
5. C.D. Rosebrock, N. Riefler, T. Wriedt, L. Mädler, S.D. Tse, AlChE J. **59**, 4553 (2013)
6. N. Jüngst, G.J. Smallwood, S.A. Kaiser, Exp. Fluids **63**, 60 (2022)
7. M. Stodt, J. Groeneveld, L. Mädler, J. Kiefer, U. Fritsching, Combust. Flame **240**, 112043 (2022)
8. M. Simmler, S. Buchheiser, R. Tischendorf, J. Poostforooshan, A.P. Weber, H.-J. Schmid, H. Nirschl, Appl. Energy Combust. Sci. **15**, 100183 (2023)
9. S. Assmann, B. Munsterjohann, F.J.T. Huber, S. Will, Materials **14**, 6698 (2021)
10. S. Aßmann, F.J.T. Huber, S. Will, Particuology **86**, 304 (2024)
11. T. Sipkens, J. Menser, T. Dreier, C. Schulz, G. Smallwood, K. Daun, Appl. Phys. B **128**, 72 (2022)
12. J. Yi, C. Betrancourt, N. Darabiha, B. Franzelli, Appl. Phys. B **129**, 97 (2023)
13. H. Dörr, *Vergleichende Untersuchung von in situ-Prozessdiagnostiken bei der Flammensynthese kleinster nanoskaliger Metalloxidpartikeln*, (Ph.D. thesis, Universität Karlsruhe, Karlsruhe 2009)
14. B. Tribalet, A. Faccinetto, T. Dreier, C. Schulz, *Evaluation of particle sizes of iron-oxide nano-particles in a low-pressure flame-synthesis reactor by simultaneous application of TiRe-LII and PMS*, (5th Workshop on Laser-induced Incandescence, Le Touquet, 2012)
15. J. Yi, C. Betrancourt, N. Darabiha, B. Franzelli, Appl. Energy Combust. Sci. **15**, 100190 (2023)
16. M. Stodt, C. Liu, S. Li, L. Mädler, U. Fritsching, J. Kiefer, Proc. Combust. Inst. **38**, 1711 (2021)
17. C. Liu, S. Li, Y. Zong, Q. Yao, S.D. Tse, Proc. Combust. Inst. **36**, 1109 (2017)
18. Y. Zhang, G. Xiong, S. Li, Z. Dong, S. Buckley, S. Tse, Combust. Flame **160**, 725 (2013)
19. H.A. Michelsen, C. Schulz, G.J. Smallwood, S. Will, Prog Energy Combust. Sci. **51**, 2 (2015)
20. J. Menser, K. Daun, T. Dreier, C. Schulz, Appl. Opt. **56**, 50 (2017)
21. G. Xiong, Y. Zhang, C. Schulz, S. Tse, Appl. Spectrosc. **76**, 569 (2022)
22. Y. Zhang, S. Li, Y. Ren, Q. Yao, S.D. Tse, Proc. Combust. Inst. **35**, 3681 (2015)
23. Y. Zhang, S. Li, Y. Ren, Q. Yao, C.K. Law, Appl. Phys. Lett. **104**, 023115 (2014)
24. Y. Ren, Y. Zhang, S. Li, Phys. Rev. Appl. **13**, 044002 (2020)
25. F. Fröde, T. Grenga, S. Dupont, R. Kneer, R. Tischendorf, O. Massopo, H.-J. Schmid, H. Pitsch, Appl. Energy Combust. Sci. **16**, 100191 (2023)
26. S.-J. Baik, P. Wollny, M. Nanjaiah, I. Wlokas, A. Kempf, Appl. Energy Combust. Sci. **15**, 100185 (2023)
27. L. Cifuentes, I. Wlokas, P. Wollny, A. Kempf, Appl. Energy Combust. Sci. **16**, 100210 (2023)
28. S. Apazeller, M. Gonchikzhapov, M. Nanjaiah, T. Kasper, I. Wlokas, H. Wiggers, C. Schulz, Proc. Combust. Inst. **39**, 909 (2023)
29. S. Apazeller, S. Karaminejad, M. Nanjaiah, H. Wiggers, T. Endres, I. Wlokas, C. Schulz, Appl. Energy Combust. Sci. **16**, 100199 (2023)
30. M. Nanjaiah, P. Wollny, P. Narasu, S. Apazeller, S. Karaminejad, T. Endres, H. Wiggers, C. Schulz, E. Gutheil, A. Kempf, I. Wlokas, Appl. Energy Combust. Sci. **15**, 100186 (2023)
31. A.M. Gadalla, H.-F. Yu, J. Mater. Res. **5**, 1233 (2011)
32. F. Schneider, S. Suleiman, J. Menser, E. Borukhovich, I. Wlokas, A. Kempf, H. Wiggers, C. Schulz, Rev. Sci. Instrum. **90**, 085108 (2019)
33. M.F.B. Stodt, J. Kiefer, U. Fritsching, Sprays **30**, 779 (2020)
34. N. Jüngst, I. Skenderović, B. Suedholt, G.J. Smallwood, F.E. Kruis, S.A. Kaiser, Appl. Energy Combust. Sci. **15**, 100167 (2023)
35. I. Skenderović, N. Jüngst, S.A. Kaiser, F.E. Kruis, Appl. Energy Combust. Sci. **15**, 100162 (2023)

36. Y. Karakaya, S. Kluge, H. Wiggers, C. Schulz, T. Kasper, Chem. Eng. Sci. **230**, 116169 (2021)
37. R. Tischendorf, M. Simmler, C. Weinberger, M. Bieber, M. Reddemann, F. Fröde, J. Lindner, H. Pitsch, R. Kneer, M. Tiemann, H. Nirschl, H.J. Schmid, J. Aerosol Sci. **154**, 105722 (2021)
38. M.R. Querry, *Optical Constants*, (Contractor Report CRDC-CR-85034, 1985)
39. P. Patnaik, *Handbook of Inorganic Chemicals* (McGraw-Hill, New York, 2003)
40. G. Ketteler, W. Weiss, W. Ranke, R. Schlögl, Phys. Chem. Chem. Phys. **3**, 1114 (2001)
41. Y.E. Mendili, J.F. Bardeau, N. Randrianantoandro, A. Gourbil, J.M. Greneche, A.M. Mercier, F. Grasset, J. Raman Spectrosc. **42**, 239 (2011)
42. S. Karaminejad, S.M.L. Dupont, M. Bieber, M.A. Reddemann, R. Kneer, T. Dreier, T. Endres, C. Schulz, Proc. Combust. Inst. **39**, 2673 (2022)
43. M.M. Prenting, *Optical and Laser-based in situ Diagnostics in Lab-scale and Pilot-scale Spray Flames for Nanoparticle Synthesis*, (Unpublished Ph.D. thesis, Universität Duisburg-Essen, Duisburg 2024)
44. W.J.A. Dahm, K.B. Southerland, K.A. Buch, Phys. Fluids **3**, 1115 (1991)
45. J.H. Frank, S.A. Kaiser, Exp. Fluids **49**, 823 (2010)
46. S.M. Mahmoud, T.C. Lau, G.J. Nathan, P.R. Medwell, Z.T. Alwahabi, B.B. Dally, Proc. Combust. Inst. **37**, 927 (2019)
47. K.P. Geigle, W. O'Loughlin, R. Hadef, W. Meier, Appl. Phys. B **119**, 717 (2015)
48. M. Köhler, K.P. Geigle, W. Meier, B.M. Crosland, K.A. Thomson, G.J. Smallwood, Appl. Phys. B **104**, 409 (2011)
49. S.-Y. Lee, S.R. Turns, R.J. Santoro, Combust. Flame **156**, 2264 (2009)
50. B. Franzelli, P. Scouflaire, S. Candel, Proc. Combust. Inst. **35**, 1921 (2015)
51. S. Pope, *Turbulent Flows* (Cambridge University Press, Cambridge, 2000)
52. G. Xiong, S. Li, Y. Zhang, S.G. Buckley, D.T. Stephen, J. Anal. Spectrom. **31**, 482 (2016)
53. H. Li, *Flame Spray Pyrolysis for Synthesizing Functional Nanoparticles: Fundamental Investigations on Single and Double Droplet Combustion*, (Ph.D. thesis, Universität Bremen, Bremen 2021)